

Optical Pumping (OP)

Using Disruption of Optical Pumping in Rubidium Gas to Investigate Atomic Energy Levels

Keenan McConkey¹

Faculty of Engineering Physics, University of British Columbia

(Dated: 20 April 2021)

Numerical simulation of Rb gas under an applied magnetic was performed to determine the separation of atomic states down to hyperfine manifolds of Zeeman sublevels. Both ⁸⁵Rb and ⁸⁷Rb isotopes of Rb were investigated. The disruption of optical pumping of an Rb sample under an applied RF field resonant with the energy level splitting of the magnetic field was found to experimentally agree with the numerical expectation for the Zeeman splitting. In the weak-field regime, theoretical *g*-factors were confirmed to a residual of at most 0.032, confirming that the Zeeman splitting is linear in this region. In the strong field regime, the residuals between numerically and experimentally determined quadratic Zeeman field splitting were at most 0.02 Gauss. Optical pumping dynamics were also compared between numerical simulation and experimental work. Data from an optically pumped Rubidium sample showed that the absorption curve follows an exponential decay relationship with the decay modulated according to the intensity of the optical light source.

I. INTRODUCTION

Optical pumping is a technique which has been well studied in physics. The basis of the method is the use of photons to induce transitions between atomic energy levels. It has been put to use in a number of fields. For example, in medicine it is used in magnetic-resonance imaging (MRI)¹, and in physical chemistry it is useful for performing spectroscopy on gasses². It is also used to achieve population inversion in the construction of lasers³. Anytime a polarized gas is needed, optical pumping is the usual way to produce it⁴.

The invention of the laser begins with Einsteins 1917 paper on quantum radiation⁵, but it was not until the 50s when French scientist Alfred Kastler proposed his method of optical pumping⁶ that its development became a reality⁷. The breakthrough was used by the American scientist Charles Townes in the creation of the maser, the first device operating on the principles proposed by Einstein⁸. Both Kastler and Townes went on to win Nobel prizes for their work, and optical pumping is now used in physics labs around the world.

II. THEORY

Throughout this paper, we concern ourselves with the optical pumping of Rubidium gas. Rb is a fairly simple atom: it has a similar electronic structure to Hydrogen and can thus be well approximated by a single-electron model. However, its nuclear properties differ from H, which affects the structure of its energy levels. There are two isotopes of Rb which commonly occur in nature, ⁸⁵Rb and ⁸⁷Rb, with abundances of 72% and 28% respectively⁴.

A. Atomic Structure

1. Electronic Structure

The simplest model of a one-electron atoms neglects the spin of both the electron and the nucleus and concerns itself only with the order in which the 37 electrons fill orbital shells:

$$1s^2 2s^2 2p^6 3s^2 3p^6 3d^{10} 4s^2 4p^6 5s^1 5p^0 \quad (1)$$

The level notation $n\ell$ denotes n , the principal quantum number, and $\ell = s, p, d, f, \dots$, the electron orbital angular momentum. For Rb, the p orbital is the first available excited states for the electron.

2. Fine Structure

The spinless model works fairly well, but high resolution spectroscopy reveals additional structures which it cannot account for. To improve our model, we must first consider the spin of the electron, $S = 1/2$, which has an associated magnetic dipole moment. This electron spin couples with the atom's orbital angular momentum, L . In the frame of the electron, the positively charged nucleus appears to be moving which induces a magnetic field. The electron interacts with this field, producing a small shift in energy. We define a new quantum number for this total angular momentum:

$$\mathbf{J} = \mathbf{L} + \mathbf{S} \quad (2)$$

Where J can take on values ranging from $L + S$ down to $|L - S|$ in integer steps. We can label these new states with a new term symbol, $^{2S+1}L_J$. Since the ground state of Rb is a $5s$ state, $L = 0$ and thus J only takes on one value, $J = 1/2$. The excited state is a $5p$ state with $L = 1$ and J can take on either $J = 1/2$ or $J = 3/2$. We denote the transitions between these fine states, $^2S_{1/2} \rightarrow ^2P_{1/2}$ and $^2S_{1/2} \rightarrow ^2P_{3/2}$, as the D_1 and D_2 transitions respectively.

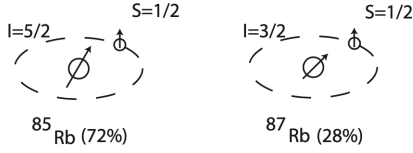


FIG. 1. The two commonly occurring isotopes of Rb found in nature, ^{85}Rb and ^{87}Rb , labelled with their respective electron spin S and nuclear spin I . Both have single-electron valence shells, but they vary in the value of their nuclear spins⁴.

3. Hyperfine Structure

Further refinements can be made to the model by also considering the spin of the nucleus, which is labelled with quantum number I . This nuclear spin again couples with the total angular momentum J , so we introduce another new quantum number:

$$\mathbf{F} = \mathbf{J} + \mathbf{I} \quad (3)$$

Where F can take on values ranging from $J+I$ down to $|J-I|$ in integer steps. At this point we need to differentiate between the two isotopes of Rb. ^{85}Rb has nuclear spin $I = 5/2$, so F can take on either $F = 3$ or $F = 2$, while ^{87}Rb has spin $I = 3/2$, which means F can take on either $F = 2$ or $F = 1$.

4. Zeeman Effect

In the absence of any external fields, each of the hyperfine levels is actually $2F + 1$ degenerate levels, which are labelled by M_F , the projection of F along some quantization axis, where $-F \leq M_F \leq F$ in integer steps. If an external magnetic field is applied, this degeneracy is broken as the magnetic dipole moment of the atom interacts with the outside field. In the case of a small magnetic field Zeeman splitting is linear and is given by:

$$E_Z = g_F \mu_B B M_F \quad (4)$$

Where $\mu_B = \frac{e\hbar}{2m}$ is the Bohr-magneton, and g_F is the hyperfine g -factor:

$$g_F = g_J \frac{F(F+1) + J(J+1) - I(I+1)}{2F(F+1)} \quad (5)$$

Where:

$$g_J = 1 + \frac{J(J+1) + S(S+1) - L(L+1)}{2J(J+1)} \quad (6)$$

In this linear weak-field regime, we can immediately observe from (4) that spacing between adjacent M_F levels is equal. Weak magnetic field means the Zeeman splitting is much less than the hyperfine splitting. For larger magnetic field, this will not be case: the Zeeman splitting will become quadratic, and the spacing between levels unequal.

The complete model of atomic structure is summarized in FIG. 4.

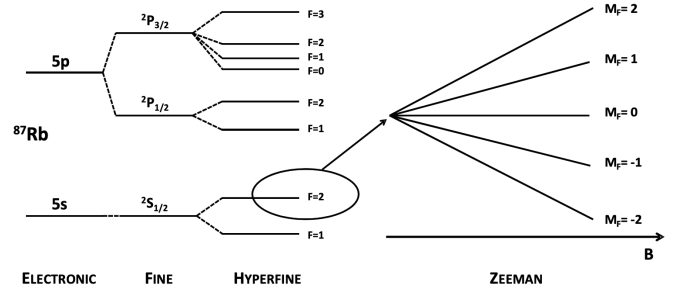


FIG. 2. Atomic structure of ^{87}Rb ($I = 3/2$), including electronic, fine, and hyperfine structure. Pictured right is the small-field Zeeman splitting as a function of magnetic field⁹. Image is not to scale.

Electron spin g -factor	g_S	2.0023193043622(15)
^{85}Rb Nuclear g -factor	g_I	-0.00029364000(60)
^{87}Rb Nuclear g -factor	g_I	-0.0009951414(10)
^{85}Rb Hyperfine constant	a_{hf}	$h \cdot 1.0119108130(20)$ GHz
^{87}Rb Hyperfine constant	a_{hf}	$h \cdot 3.417341305452145(45)$ GHz

TABLE I. g -factors and hyperfine constants for both Rb isotopes^{10,11}.

B. Finding the Eigen Energies

In order to numerically determine the energy spectrum of our Rb system, we solve the time-independent Schrodinger equation.

$$\hat{H}|\Psi\rangle = E|\Psi\rangle \quad (7)$$

Where \hat{H} is the Hamiltonian, E is the energy eigenvalue, and $|\Psi\rangle$ is the eigenvector of the Hamiltonian operator. In the single-electron atom model, the only degrees of freedom are the electron spin and nuclear spin, so the Hamiltonian representing the energy of the atom is given by:

$$\hat{H} = \hat{H}_B + \hat{H}_{\text{hf}} \quad (8)$$

Where \hat{H}_B and H_{hf} are the Hamiltonians of the magnetic field and hyperfine interactions respectively. We assume without loss of generality that the magnetic field operates entirely along the z direction, so $\vec{B} = B_0 \hat{z}$. We introduce \hat{S} and \hat{I} , the vector operators of the electron and nucleus spins respectively and rewrite \hat{H}_B in terms of these quantities:

$$\hat{H}_B = \frac{\mu_B}{\hbar} (g_S \hat{S}_z + g_I \hat{I}_z) B_0 \quad (9)$$

Where g_S and g_I are the electron and nuclear spin g -factors, as listed in TABLE I. The hyperfine interaction can also be written in terms of these operators.

$$\hat{H}_{\text{hf}} = \frac{a_{\text{hf}}}{\hbar^2} \hat{S} \cdot \hat{I} = \frac{a_{\text{hf}}}{\hbar^2} (\hat{S}_x \hat{I}_x + \hat{S}_y \hat{I}_y + \hat{S}_z \hat{I}_z) \quad (10)$$

Where a_{hf} is the hyperfine constant and is also given in TABLE I. We see that we can use the tensor products of the eigenvectors of the \hat{S} and \hat{I} operators as a basis. These

vectors $|S, m_S\rangle$ and $|I, m_I\rangle$ must satisfy:

$$\begin{aligned}\hat{S}_z |S, m_S\rangle &= \hbar m_S |S, m_S\rangle \\ \hat{I}_z |I, m_I\rangle &= \hbar m_I |I, m_I\rangle\end{aligned}\quad (11)$$

The tensor product of these vectors is:

$$|S, m_S\rangle \otimes |I, m_I\rangle = |m_S, m_I\rangle \quad (12)$$

We can then represent \hat{H}_B as a diagonal matrix in this basis, with diagonal elements:

$$\langle m'_S, m'_I | \hat{H}_B | m_S, m_I \rangle = \mu_B B_0 (g_S m_S + g_I m_I) \delta_{m'_S, m_S} \delta_{m'_I, m_I} \quad (13)$$

The \hat{H}_{hf} matrix is not diagonal in this basis, but we can still find its elements. We first define the raising and lowering operators S_+ and S_- :

$$\begin{aligned}S_+ &\equiv S_x + iS_y \\ S_- &\equiv S_x - iS_y\end{aligned}\quad (14)$$

Which allows us to rewrite \hat{H}_{hf} as:

$$\hat{H}_{\text{hf}} = \frac{a_{\text{hf}}}{\hbar^2} \left(I_2 (S_+ I_- + S_- I_+) + \hat{S}_z \hat{I}_z \right) \quad (15)$$

The matrix elements of the \hat{H}_{hf} in our basis are given in (16).

By using (13) and (16) to numerically compute the complete Hamiltonian and solving for the eigen-energies, we determined the 8 and 12 magnetic sublevel energy spectra of ground state ^{85}Rb and ^{87}Rb respectively in an external magnetic field. Results for ^{85}Rb and ^{87}Rb are shown in FIG. 3. For both isotopes the sublevels are grouped into two hyperfine manifolds, which correspond to the angular momenta quantum numbers, F , available to each respective isotope ($F = 2, 3$ for ^{85}Rb and $F = 1, 2$ for ^{87}Rb). We note that the Zeeman splitting follows $-F \leq M_F \leq F$ as expected. Also shown in FIG. 3 is the small-field Zeeman splitting according to (4). We see that (4) holds when the Zeeman splitting is much less than the hyperfine splitting (which is on the order of 10^0 GHz), but diverges to quadratic splitting once this limit is broken around 100 Gauss.

C. Finding RF Transition Frequencies

Of critical interest to the experimental work is the transition frequencies between the magnetic sublevel quantum states in the applied magnetic field. Since experimentally available RF frequencies are on the MHz scale, only transitions with $\Delta F = 0$ and $\Delta M_F = \pm 1$ are of interest, i.e. transitions between states within the same hyperfine manifold. Using the computations of Section II B, we can compute these transition frequencies numerically. Results for the strong-field limit are shown in FIG. 4.

We see that the transition frequencies are degenerate in the weak-field limit, matching the expectation of equal sublevel spacing according to (4). From a linear fit to the transition frequency vs. magnetic field strength line, we confirmed that

the slope matches $g_F \mu_B / \hbar$. In the strong field limit, the results confirm that the degeneracy is broken by the applied magnetic field, as the linear Zeeman splitting becoming quadratic. We notice that there is still degeneracy between the F hyperfine manifolds of each isotope, resulting in only 6 and 4 distinct RF resonances for ^{85}Rb and ^{87}Rb respectively.

D. Photon Absorption

When a photon incident on an Rb atom has an energy that matches the spacing between two atomic energy levels, (and the lower level is inhabited by an electron), the electron is excited to the higher energy level. There are particular rules for the F and M_F levels between which transitions can occur.

The two types of transitions of interest to the experiment are shown in FIG. 5. The first type are the D_1 transitions between hyperfine levels in $^2S_{1/2}$ to another hyperfine level in the $^2P_{1/2}$ manifold. These D_1 transition are triggered by optical light in the near IR at 795 nm. The second type are triggered by an RF field on the order of kHz or MHz. The splitting between different hyperfine levels in the ground state is on the order of several GHz, so this RF radiation only drives transitions with $\Delta F = 0$. That is, only between different Zeeman levels within the same hyperfine manifold.

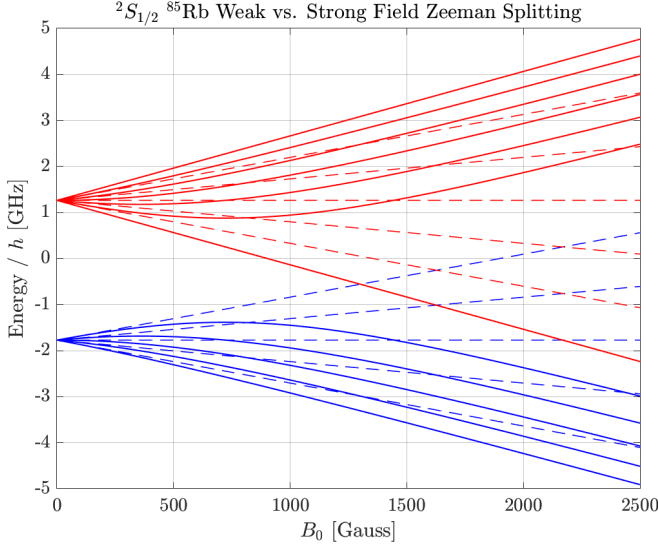
E. Optical Pumping

An incoming photon will drive transitions with either $\Delta M_F = 1$ or -1 depending on whether the light is right-circularly polarized (RCP) or left-circularly polarized (LCP). However, when the electron decays from an excited state, the transition can have any of $\Delta M_F = 0, \pm 1$. This means the average decay event will have $\Delta M_F = 0$, while every absorption event will have $\Delta M_F = +1$ (if we use RCP light), eventually causing the electrons to be pumped to the ground state with the highest M_F value, known as the stretched state.

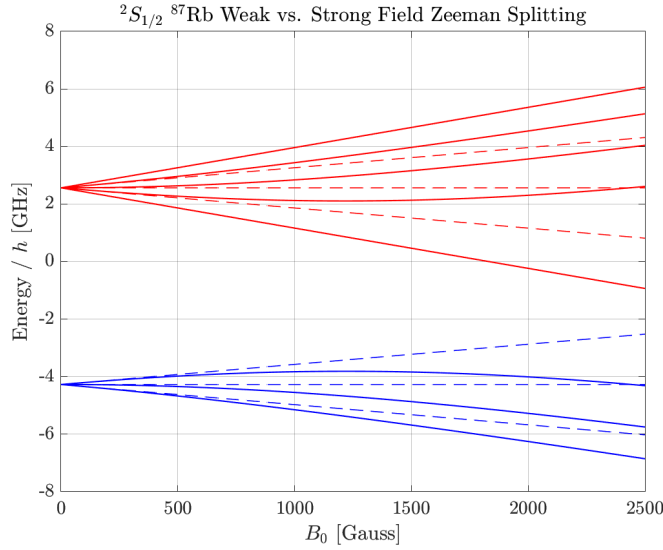
Theoretically, given enough time all atoms would end up in the final stretched. However, due to processes such as the collision between Rb atoms, optical pumping establishes an equilibrium in which more atoms are in the stretched state than there would be in the absence of light. This stretched state will be a dark state, that is, a state where an atom is no longer able to absorb a photon. This allows us to measure the occupation of the stretched state based on light intensity once the incoming light passes through the Rb cell.

Since the RF field drives transitions between different M_F states within the same hyperfine F manifold, RF can drive transitions into and out of the dark state even if the sample is fully optically pumped, reducing the number of atoms in the dark state. Thus, for a particular RF frequency, an applied magnetic field strength can be found where the energy difference between Zeeman levels matches the energy of the RF photons. This results in a loss of atoms from the dark state can be measured via a decrease in the optical light intensity transmitted through the cell, allowing for a quantitative measurement of the Zeeman splitting.

$$\begin{aligned}
\langle m'_S, m'_I | S_+ I_- | m_S, m_I \rangle &= \hbar^2 \sqrt{(S - m_S)(S + m_S + 1)(I + m_I)(I - m_I + 1)} \delta_{m_S+1, m'_S} \delta_{m_I-1, m'_I} \\
\langle m'_S, m'_I | S_- I_+ | m_S, m_I \rangle &= \hbar^2 \sqrt{(S + m_S)(S - m_S + 1)(I - m_I)(I + m_I + 1)} \delta_{m_S-1, m'_S} \delta_{m_I+1, m'_I} \\
\langle m'_S, m'_I | \hat{S}_z \hat{I}_z | m_S, m_I \rangle &= \hbar^2 m_S m_I \delta_{m_S, m'_S} \delta_{m_I, m'_I}
\end{aligned} \tag{16}$$

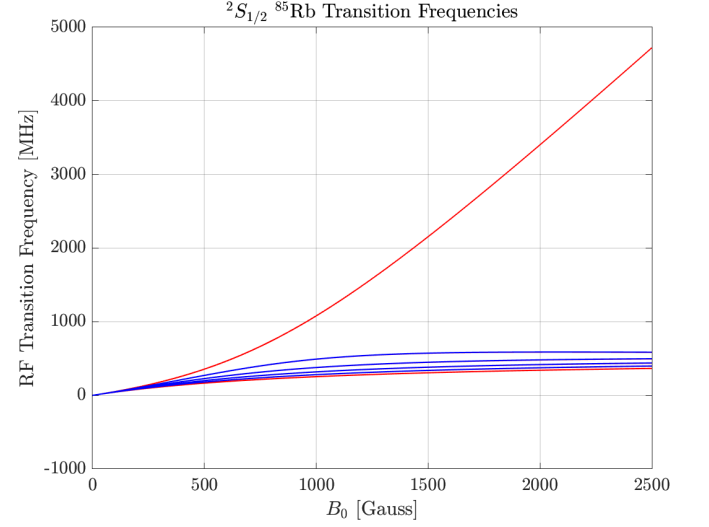


(a)

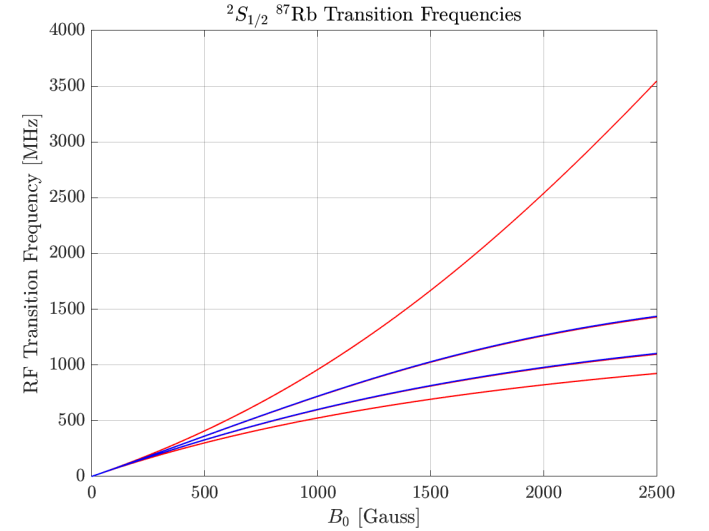


(b)

FIG. 3. Numerical simulation of the Zeeman splitting of hyperfine levels of ^{85}Rb (a) and ^{87}Rb (b) due to an applied magnetic field. The Hamiltonian solution is compared to the linear approximation (4). The two manifolds in each isotope correspond to hyperfine F levels with sublevels following $-F \leq M_F \leq F$. Note the divergence of Zeeman splitting from the linear approximation when the Zeeman splitting is no longer small compared to hyperfine levels.



(a)



(b)

FIG. 4. Numerical simulation of the transition frequencies for both Rb isotopes. The transitions are degenerate and linear in the weak-field limit but expand in the strong-field due to the onset of quadratic Zeeman splitting. Notice the degeneracy between the two F hyperfine manifolds, which results in only 6 and 4 distinct RF resonances for ^{85}Rb and ^{87}Rb respectively.

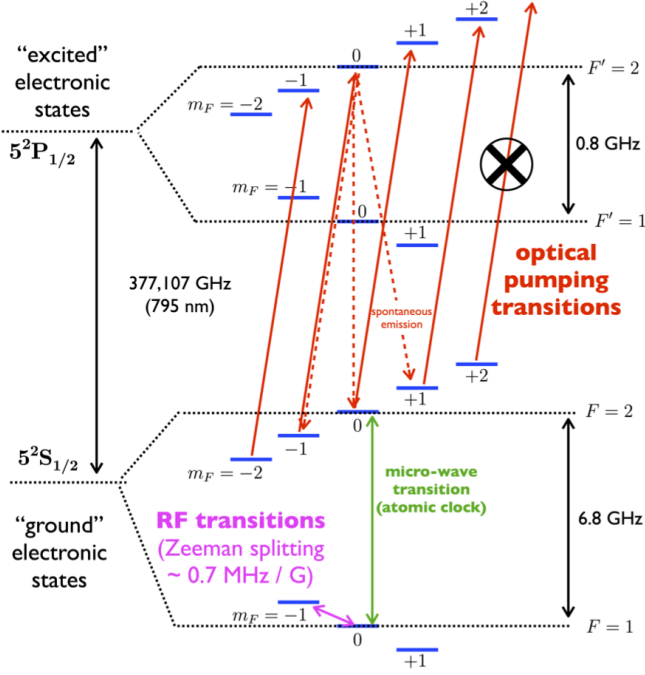


FIG. 5. Atomic energy level of the ^{87}Rb atom and the transitions driven by optical light and by radio frequency (RF) field. Optical pumping drives transitions between the hyperfine states with $\Delta M_F = +1$, which eventually causes the Rb gas sample to stop absorbing light. An RF coil operating between 10 kHz and 10 MHz drives transitions between the Zeeman sublevels of the hyperfine states, which disrupts optical pumping. This allows us to investigate the nature of Zeeman splitting through observation of optical pumping disruption for varying magnetic field strengths and RF coil frequencies⁹.

F. Dynamics of Optical Pumping

We now consider the dynamics of optical pumping, i.e. how fast incoming photons actually pump an Rb sample into its stretched state. For simplicity but without loss of generality, we concern ourselves with the D_1 transition line of ^{87}Rb between excited and ground states. We also assume that the incoming optical is LCP, such that only $\Delta M_F = -1$ transitions are allowed and resonant with the allowed transitions. The system consists of two ground states with angular momenta $F = 1$ and $F = 2$ and two excited states with $F' = 1$ and $F' = 2$.

Based on the possible combinations of F and M_F , we come up with $|F, M_F\rangle \equiv |k\rangle$ excited states denoted by index k and $|F, M_F\rangle \equiv |i\rangle$ ground states denoted by index i , where $i, k \in 1, 2, \dots, 8$. We can then describe the relative number of atoms in the excited and ground states, N_k and N_i , via rate equations:

$$\begin{cases} \dot{N}_k = \sum_i P_{ik} (N_i - N_k) + \sum_i \Gamma_{ik} N_i \\ \dot{N}_i = \sum_k P_{ik} (N_k - N_i) - \sum_k \Gamma_{ik} N_i \end{cases} \quad (17)$$

Where P_{ik} is the rate at which stimulated pumping transitions proceed and Γ_{ik} is the rate at which spontaneous transitions occur. Both rates are governed by the matrix elements of the

dipole operator, which using the Wigner-Eckart theorem, we can factor into:

$$|d_{ik}|^2 = |\langle J' | er | J \rangle|^2 \times f_{ik} \equiv d^2 \times f_{ik} \quad (18)$$

Where f_{ik} are the oscillator strengths of individual $i \leftrightarrow k$ transitions and d is connected to the life time τ of the whole excited manifold via:

$$d^2 = \frac{1}{\tau} \frac{6\pi\epsilon_0\hbar c^3}{\omega_0^3} \quad (19)$$

For the ^{87}Rb D_1 transition line, $\tau = 27.68$ ns and $\omega_0 = 2\pi \cdot 377.10746338\text{THz}$. f_{ik} can be solved for via angular momenta algebra:

$$f_{ik} = \begin{pmatrix} 1/12 & 1/12 & 0 & 1/2 & 1/4 & 1/12 & 0 & 0 \\ 1/12 & 0 & 1/12 & 0 & 1/4 & 1/3 & 1/4 & 0 \\ 0 & 1/12 & 1/12 & 0 & 0 & 1/12 & 1/4 & 1/2 \\ 1/2 & 0 & 0 & 1/3 & 1/6 & 0 & 0 & 0 \\ 1/4 & 1/4 & 0 & 1/6 & 1/12 & 1/4 & 0 & 0 \\ 1/12 & 1/3 & 1/12 & 0 & 1/4 & 0 & 1/4 & 0 \\ 0 & 1/4 & 1/4 & 0 & 0 & 1/4 & 1/12 & 1/6 \\ 0 & 0 & 1/2 & 0 & 0 & 0 & 1/6 & 1/3 \end{pmatrix} \quad (20)$$

Using we (19) and (20) we can write down equations for the stimulated transition rate:

$$P_{ik} = \left(\frac{E d_{ik}}{\hbar} \right)^2 \tau C_{ik} = \frac{6\pi c^2}{\hbar \omega_0^3} I f_{ik} C_{ik} \quad (21)$$

Where I is the intensity of the incoming light and E is the electric field amplitude, which are related via $I = c\epsilon_0 E^2$. The spontaneous transition rate is:

$$\Gamma_{ik} = \frac{1}{\tau} f_{ik} \quad (22)$$

C_{ik} is the selection matrix for LCP light, i.e. $M'_{F'} = M_F - 1$. Explicitly:

$$C_{ik} = \begin{pmatrix} 0 & 1 & 0 & 0 & 0 & 1 & 0 & 0 \\ 0 & 0 & 1 & 0 & 0 & 0 & 1 & 0 \\ 0 & 0 & 0 & 0 & 0 & 0 & 0 & 1 \\ 1 & 0 & 0 & 0 & 1 & 0 & 0 & 0 \\ 0 & 1 & 0 & 0 & 0 & 1 & 0 & 0 \\ 0 & 0 & 1 & 0 & 0 & 0 & 1 & 0 \\ 0 & 0 & 0 & 0 & 0 & 0 & 0 & 1 \\ 0 & 0 & 0 & 0 & 0 & 0 & 0 & 0 \end{pmatrix} \quad (23)$$

A complete picture of the possible transmissions between energy levels for the D_1 line of ^{87}Rb is shown in FIG 6.

By substituting (21) and (22) into rate equation (17), we can numerically compute the state populations as a function of time. The results for $I = 1$ mW/cm² and $I = 10$ mW/cm² are shown in FIG. 7. Simulation begins with an isotropic population distribution among ground state sublevels ($N_k = 1/8 \forall k$) and empty excited state ($N_i = 0 \forall i$). We confirm that given enough time, the theoretical (i.e. not worrying about atom-atom interaction) system completely collapses into the dark (stretched) state.

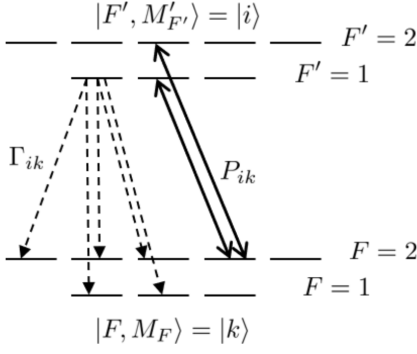


FIG. 6. Energy level diagram⁹ of the D_1 line of ^{87}Rb . Bold arrows depict the possible stimulated transmissions originating from ground state $|F=2, M_F=1\rangle$, while dashed arrows depict the possible spontaneous transmissions originating from excited state $|F'=1, M'_{F'}=-1\rangle$.

Excited states are filled for a short time by optical pumping, but quickly transition back to ground states. At each spontaneous transition some atoms end up in the dark state; since atoms cannot escape this dark state via optical pumping eventually all end up there. The time scale of this dark state filling is dictated by the intensity of the optical pumping source light. Intensity is directly proportional to energy transfer into the system so higher intensity stimulates more transmissions. Since this means the excited states fill faster, they also decay back into ground states more quickly.

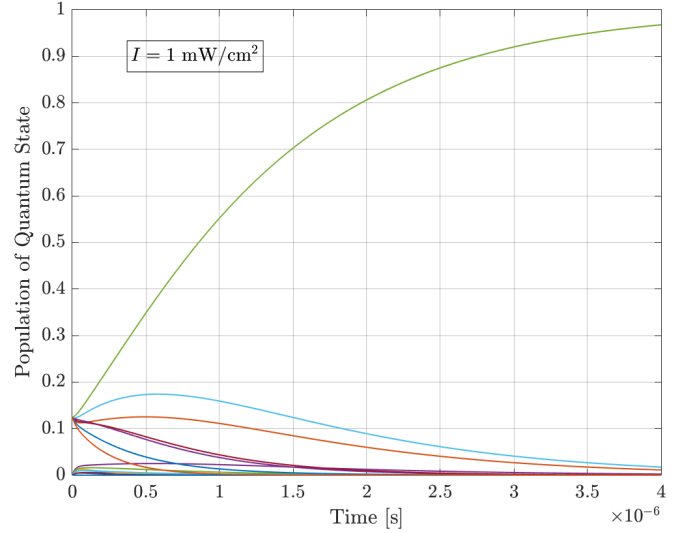
G. Absorption Dynamics

In order to numerically determine the experimental observable, the absorption of ^{87}Rb gas as a function of time under continuous excitation by a light source tuned to the frequency of the D_1 transition, we multiply the ground state occupation function $N_k(t)$ by the stimulated transition summed over all absorption channels, $\sum_i P_{ik}$. The result for varying intensity is given in FIG. 8. Absorption is an exponential decay curve in time. For higher intensity, absorption decays faster, as the dark state is filled more quickly. There is a limit to the absorption decay speed however. Past about $I = 100 \text{ mW/cm}^2$ the absorption vs time curve collapses to an exponential decay starting at 50% absorption. Intensities equal to or greater than $I = 100 \text{ mW/cm}^2$ immediately transition all the ground states to excited states, half of which quickly decay back into the dark ground state, which is why we see the 50% absorption starting point.

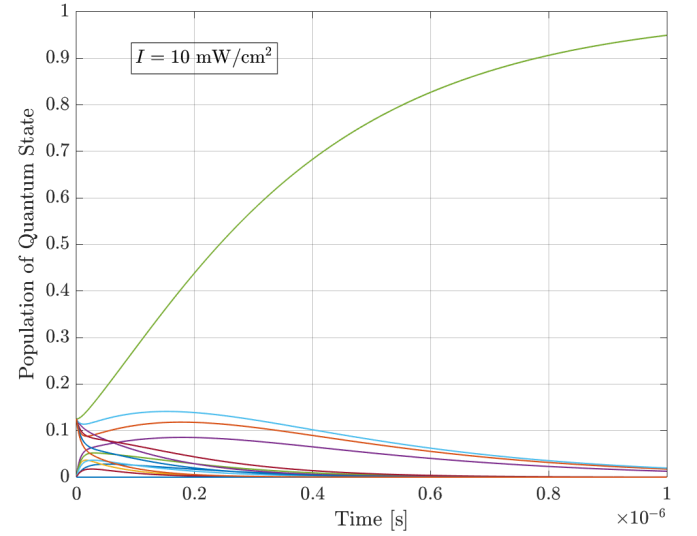
III. EXPERIMENT

A. Apparatus

The hardware used in this experiment is shown in FIG. 9. Light at 780 nm and 795 nm is produced by a Rb vapor in



(a)



(b)

FIG. 7. Numerical simulation of optical pumping dynamics for intensities $I = 1 \text{ mW/cm}^2$ and $I = 10 \text{ mW/cm}^2$. As expected, given enough time the system entirely collapses into the dark states, from which simulated transmission cannot occur. Intensity dictates the time scale of this collapse (note the difference in time scale between the graphs).

the lamp on the left of the image. A lens focuses the light into the Rb cell. Before it enters the lens the light passes through a series of optical instruments: an interference filter which blocks the 780 nm light but allows the 795 nm light to pass; then a linear polarizer and quarter wave plate combination which outputs circularly polarized light. When the light hits the Rb cell some of it is absorbed by the atomic vapour, the rest passes to a collecting lens where it is focused onto the optical detector on the right of the image. This optical detector produces a voltage proportional to the amount of light that gets through the cell, which is recorded by an oscilloscope.

The magnetic field in the sample (along the z direction) is

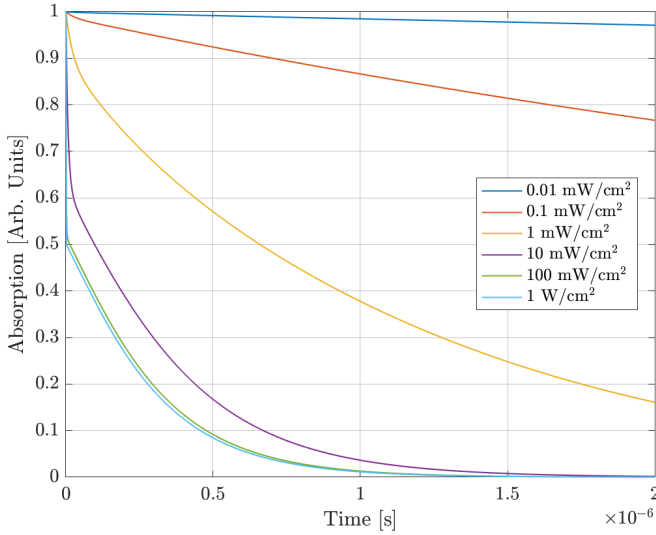


FIG. 8. Absorption decay curves at intensity values ranging from $I = 0.01 \text{ mW/cm}^2$ to $I = 1 \text{ W/cm}^2$. Absorption decays faster for higher intensities, up until a "speed-limit" past about $I = 100 \text{ mW/cm}^2$, where the decay collapses into a curve starting at 50% absorption.

controlled through a combination of the main horizontal coil and the horizontal sweep coil. The main coil can be set in order to bias the magnetic field strength in the sample to a minimum value. The sweep coil is then used to finely probe the magnetic field strengths beyond the bias field. An oscillating RF field is produced in the y direction by the RF coil shown in the image. Both the magnetic field strength and the RF coil frequency are controlled by an amplifier system not shown. By setting the main coil to a particular bias field and RF coil to a particular frequency, Zeeman splitting can be observed precisely.

B. Sources of Noise and Uncertainty

There are numerous possible sources of noise in the experiment. The most likely is the uncertainty introduced by the coils used to generate magnetic field. In Section IV B, we calibrate the current input into these coils to the magnetic field they produce. This results in relative uncertainties of 0.78% and 0.13% in the calibration of the sweep and main coils respectively, which we round up to a relative uncertainty of 1% in the total magnetic field generated by the combined action of the sweep and main coil.

This result tends to underestimate the actual fluctuation in the Zeeman splitting data. Further fluctuation has to be accounted for due to noise in the current generated in the main coil. That is, there is a systematic fluctuation between the current set in the main coil and the actual current produced, which leads to a fluctuation in the magnetic field it produces that is greater than the fluctuation accounted for by calibration. By manually correcting this fluctuation in the collected data (Section IV C), this fluctuation was found to average $\sigma(B_{\text{main}}) = 0.178 \text{ Gauss}$, with a maximum deviation

of 0.282 Gauss (see TABLE III). Once this fluctuation is accounted for, experimental Zeeman splitting matches numerical predictions well within uncertainty.

Other sources of noise and uncertainty are possible. The RF frequency band is often used for wireless communications, so man-made noise in this band can occur¹². There is a small uncertainty in reading the sweep coil field due to discretization of the oscilloscope, which amounts to 10^{-2} Gauss i.e. much less than the other coil uncertainties. The uncertainty in the optical detector is unimportant as we only observe the pattern of absorptions rather than a specific quantity. Finally, any light source has a variation in its emission rate, due to quantum noise (i.e. the random nature of photon emission)¹³, but this is unlikely to have an effect at the intensity scales we use in our experiment.

IV. RESULTS

A. Confirming G-Factors

The first step of experimental analysis was to confirm the experimental values of the hyperfine g -factors, as seen in (4). Using data collected for four RF frequencies in the 60-180 kHz range with zero main coil current (the weak-field regime), resonant magnetic fields in both ^{85}Rb and ^{87}Rb were determined based on where optical pumping was disrupted in the optical detector data. Background field strength was calculated to be $B_{\text{bg}} = 0.1854 \text{ Gauss}$ and was subtracted from the field calculated off the sweep coil current to obtain the resonant field strength for each resonant frequency. By extracting the slopes of this frequency to field strength relationship for each isotope independently and relating them to (4), we obtained experimental g -factors for both isotopes

$$\begin{aligned} g_{F,85} &= 0.3289 \\ g_{F,87} &= 0.4689 \end{aligned} \quad (24)$$

The frequency vs field strength relationship and obtained linear fits for both isotopes are shown in FIG. 11. Uncertainty can be directly propagated from the residuals of the slope for each isotope, resulting in:

$$\begin{aligned} \sigma(g_{F,85}) &= \pm 0.0035 \\ \sigma(g_{F,87}) &= \pm 0.0042 \end{aligned} \quad (25)$$

According to (5), the theoretical g -factors are $g_F = 1/3$ for ^{85}Rb and $g_F = 1/2$ for ^{87}Rb . The residuals between the theoretical and experimental g -factors is at most 0.032. The uncertainty range of the experimental results are outside the theoretical value for ^{87}Rb , but we are close enough to use the theoretical g -factors going forward.

B. Calibration of the Current-Field Relationship

With g -factors confirmed, a calibration relationship between both the coil current and generated field in both the

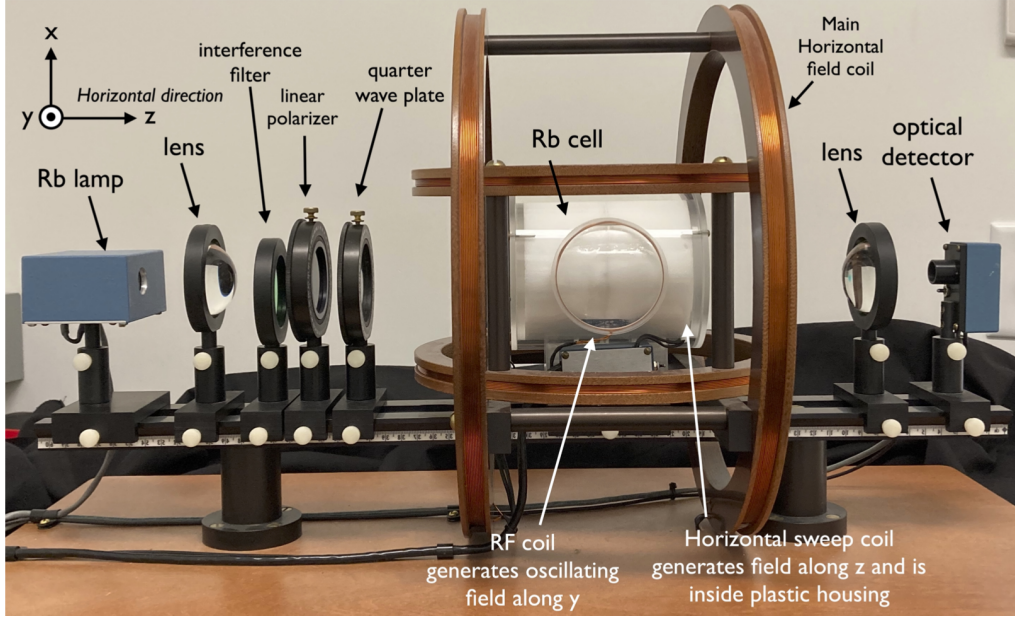


FIG. 9. The apparatus used in the optical pumping experiment⁹. The Rb lamp (far left) generates light at 780 nm and 795 nm. After being focused by passing through a lens, the light hits an interference filter which removes the light at 780 nm, then a linear polarizer and quarter wave plate series which circularly polarizes the light. When the light hits the Rb cell sample, some of the light is absorbed by the vapour; the rest passes through and is focused by a second lens onto an optical detector. The DC magnetic field in the z direction is controlled by a combination of a main horizontal coil and a sweep coil, which allows for precise magnetic field tuning. An oscillating field in the y direction is created by the RF coil.

sweep and main coil must be determined¹⁴. For set values of the RF coil frequency, the expected transition magnetic field strength can be calculated by rearranging (4):

$$B_{\text{RF}} = \frac{h\nu_{\text{RF}}}{g_F\mu_B} \quad (26)$$

By computing expected transition field strengths from (26) and comparing to the coil current at which transitions are observed in experimental optical pumping data, a calibration relationship for both coils can be determined. The calibration the sweep coil was done by calculating the magnetic field using (26). The main coil calibration was done after the sweep coil current had been calibrated, with main coil magnetic field calculated via:

$$B_{\text{main}} = B_{\text{total}} - B_{\text{sweep}} = \frac{\nu_{\text{RF}}}{g_F} \frac{h}{\mu_0} - B_{\text{sweep}} \quad (27)$$

The resulting calibration fits for both the main and sweep coil are shown in FIG. 11. The intercept of the main coil calibration is near zero so it is approximated as such. The linear calibration fits are:

$$\begin{aligned} B_{\text{sweep}} &= 0.5749 \cdot I_{\text{sweep}} - 0.1536 \quad (\text{Gauss}) \\ B_{\text{main}} &= 8.799 \cdot I_{\text{main}} \quad (\text{Gauss}) \end{aligned} \quad (28)$$

The uncertainty can again be directly propagated from the residuals of the slope, resulting in relative uncertainties of 0.78% and 0.13% for the sweep and main coils respectively. We round this up to a total uncertainty of 1% when using the calibration of the sweep and main coils combined.

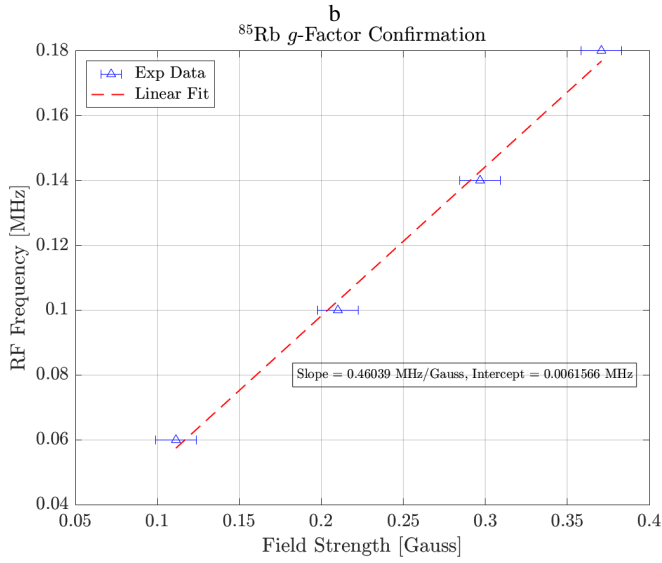
C. Analysis of Strong Field Zeeman Splitting

Using the sweep and main coil calibrations of (28), we can now investigate the onset of quadratic Zeeman effect in the strong-field regime. Using magnetic field scans at various fixed RF frequencies, we can compare the magnetic field to RF frequency relationship in the strong-field case to the numerical results of Section II B. We note that the total magnetic field generated by the coils is given by:

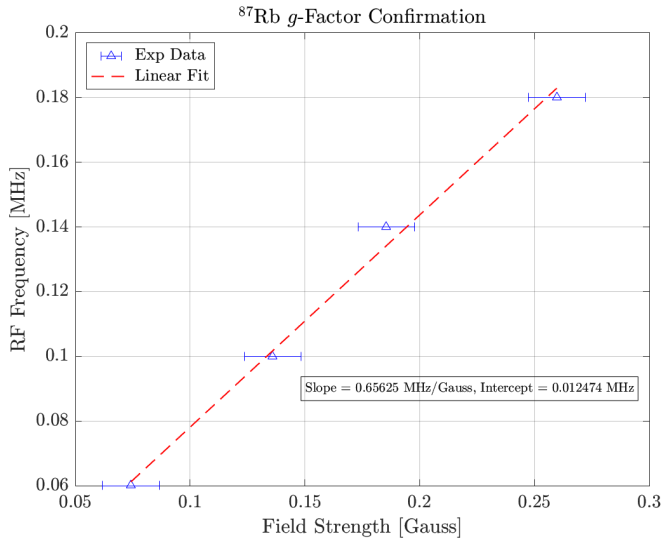
$$B_{\text{total}} = B_{\text{main}} + B_{\text{sweep}} \quad (29)$$

The results of numerical simulation vs experimental data across the full range of sample frequencies is shown in FIG. 12. From qualitative observation, we see that these experimental results match the curve of the numerical lines. As expected, strong fields break the degeneracy of the Zeeman splitting, resulting in quadratic transitions frequencies. There are deviations in the experimental results due to systematic fluctuations in the output of the main coil, the nature of which is discussed in detail in Section III B. By zooming on each of the RF frequencies used in data collection, this systematic main coil error can be corrected for, and the experimental result can be compared to the expected Zeeman splitting for a set RF frequency. An example of zoomed-in, main-coil corrected Zeeman effect observation is shown in FIG. 13. The error-bars are computed from the calibration in (28).

The results of the systematic field correction needed for each of the observed RF frequencies is summarized in TABLE II. From these results, we conclude that the average system-



(a)



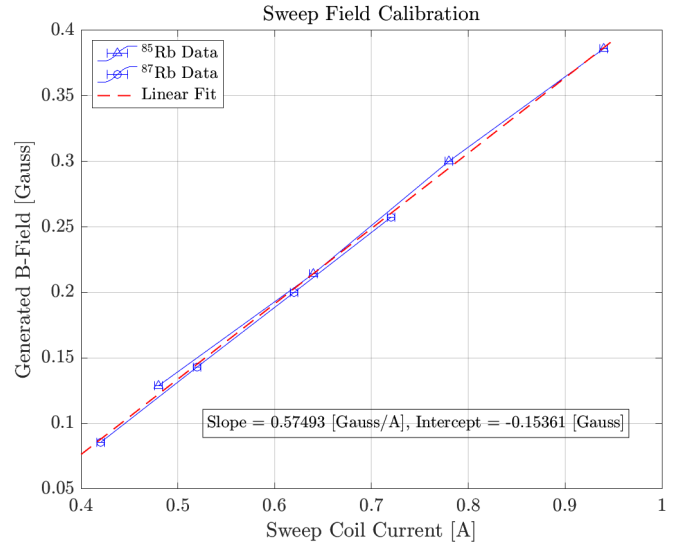
(b)

FIG. 10. Experimental confirmation of the g_F -factors of both ^{85}Rb (a) and ^{87}Rb (b). This was done by determining resonant magnetic field strength for particular RF frequencies in the weak-field (zero main coil bias) regime and comparing the resulting frequency to field strength relationship to that of (4).

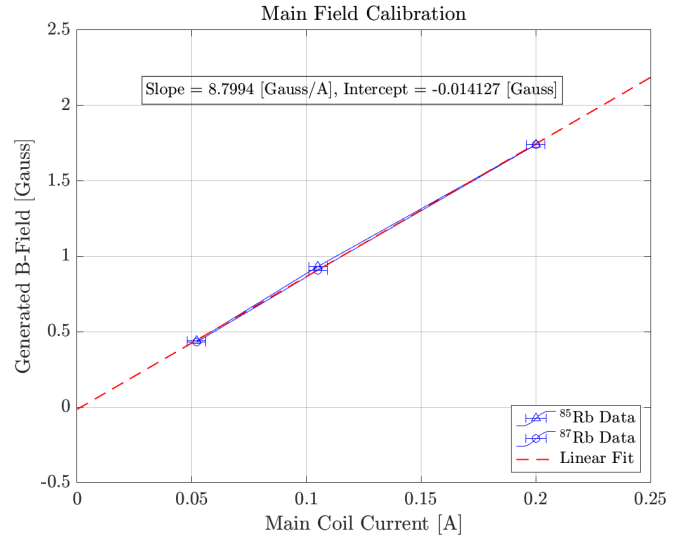
atic fluctuation in main coil output is 0.1778 Gauss. Once the systematic fluctuation is accounted for, the residual between the numerical and experimental magnetic field strength splitting due to the Zeeman effect is at most 0.02 Gauss.

D. Dynamics of Optical Pumping

To investigate the dynamics of optical pumping, we have collected data in which a sample is initially being pumped but an RF field turned ON is preventing optical pumping, which results in a low optical detector signal. When the RF sig-



(a)



(b)

FIG. 11. Calibration of the sweep coil and main field by relating the expected transition magnetic field for a set of RF frequencies to the coil current at which optical pumping is disrupted. The result is a linear current-to-field-generated relationship for both the main and sweep coil, with a combined relative uncertainty of 1%.

Observed RF Frequency (MHz)	Main Field Fluctuation (Gauss)
7.2	-0.140
10.85	-0.135
5.8	0.080
8.68	0.080
4.62	-0.278
3.05	-0.282
2.2	0.163
3.1	0.137

TABLE II. Main coil field fluctuations at each of the observed RF frequencies.

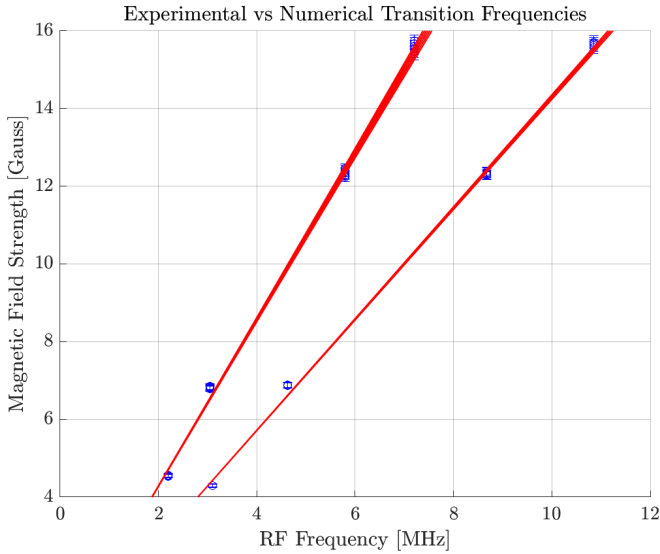


FIG. 12. Numerical (red) vs experimentally determined (blue) transition magnetic field strengths for observed values of RF frequencies. The left line corresponds to the ^{85}Rb isotope, while the right line corresponds to ^{87}Rb . As expected from the results of numerical simulation, in the strong-field regime, Zeeman effect causes the transition frequencies to become non-degenerate and linear. A systematic magnetic field strength fluctuation can be observed, which needs to be corrected for at each observed RF frequency.

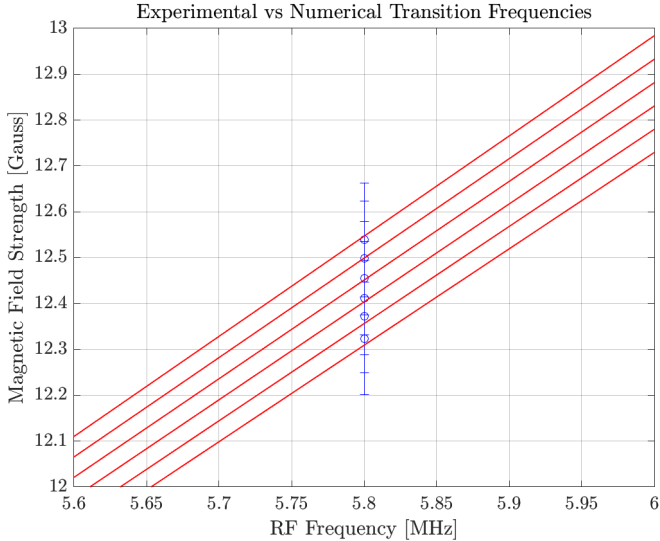


FIG. 13. Close up of the magnetic field strength splitting of a single observed RF frequency (5.8 MHz), comparing numerical simulation (red) to experimental (blue) data. The transition lines are for the ^{85}Rb isotope. After correcting for a systematic main coil error, the magnetic field resonances align with a residual of at most 0.02 Gauss.

nal is suddenly switched OFF, optical pumping begins and drives the atoms to the dark states, where the detector signal increases to the well-pumped steady state.

By fitting exponentials to the observed absorption decay curves in the detector signals, we extracted the time constants for the rate at which optical pumping proceeds. An example

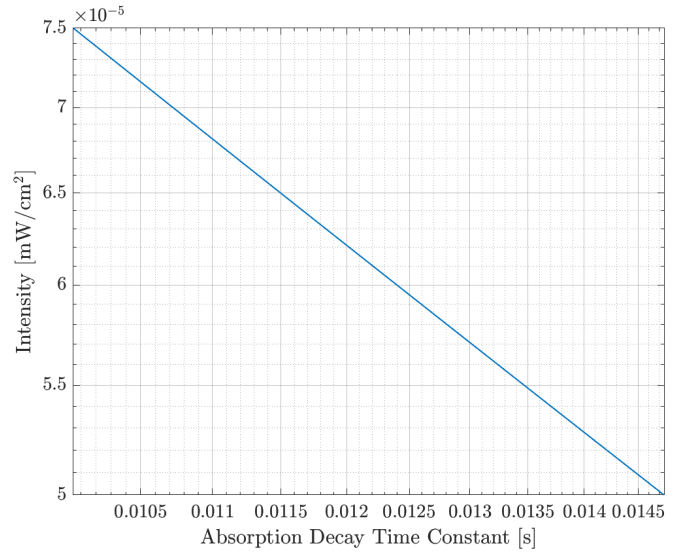


FIG. 14. Simulation of the intensity vs. absorption-decay time constant curve in the range near the experimentally observed time constants. For small intensity, the relationship becomes linear in the log-log space, allowing us to easily infer intensities from the experimental time constants.

of an absorption decay curve with its fit exponential is shown in FIG. 15. The process was done for three polarizer angles: 45° , 65° , and 80° . Using the numerical predictions of II G, the extracted time constants were matched to corresponding input beam intensities. An absorption curve was simulated near the range of the observed time constants, resulting in a linear line in log-log space, as shown in FIG 14.

The results of the time constant extraction and conversion to input beam intensity using FIG 14 are shown in TABLE III. The time constant uncertainties are calculated using the 95% confidence interval output from the exponential fitting function, which corresponds to a k factor of $k \approx 2$. The propagation of the time constant uncertainty to intensity uncertainty is given by:

$$\sigma(I) = \sigma(\text{TC}) \cdot \frac{I \log^2(I)}{\text{TC}} \quad (30)$$

V. CONCLUSIONS

In summary, we reproduced the results of numerical simulations of the Zeeman effect on hyperfine levels in experimental findings. In the weak field case, the splitting was observed to be linear with degenerate transition frequencies according to (4), which was confirmed by matching the g_F factors with a residual of at most 0.032:

$$g_{F,85} = 0.329 \pm 0.004$$

$$g_{F,87} = 0.469 \pm 0.004$$

In the strong field limit, simulation quadratic Zeeman splitting was found to predict the transition frequencies with a residual

Polarizer Angle (°)	Time Constant (ms)	Uncertainty (ms)	Intensity ($\mu\text{W}/\text{cm}^2$)	Uncertainty (nW/cm^2)
45	14.5	0.11	51.7	6.1
65	12.0	0.088	62.1	7.7
80	10.5	0.074	71.5	9.2

TABLE III. Time constants and intensities for varying polarizer angles determined by fitting an exponential decay curve to the experimental absorption decay data.

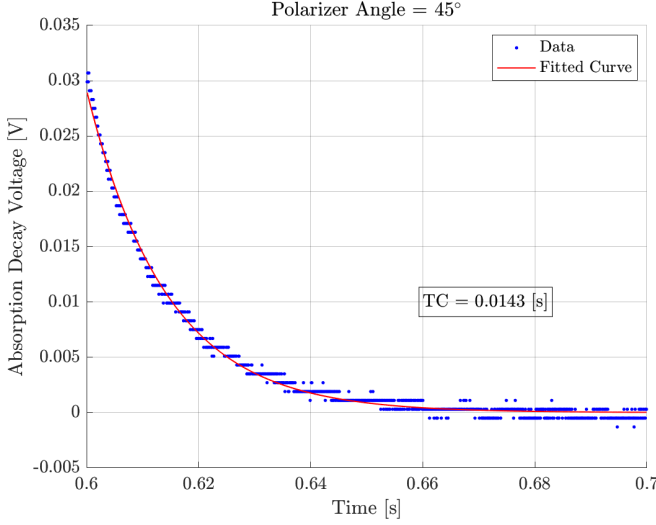


FIG. 15. Absorption decay curve with fitted MATLAB curve-fitting exponential used to extract the absorption decay time constant. The extracted time constant is 0.0143 seconds. We can use numerical results to match an intensity value to this observed time constant.

of at most 0.02 Gauss, after correcting for a systematic fluctuation in the main coil (see TABLE II). This required calibration of the coil to field generated relationship in both the main and sweep coils via matching of expected resonant transition field strengths, which is given in (28).

In optical pumping dynamics, simulation of the rate equations of the ground and excited states of the $^{87}\text{Rb } D_1$ transition line was found to predict the absorption decay curve observed experimentally through manipulation of the ON state of an RF coil. Exponential functions were fit to the absorption decay curves in order to extract absorption time constants. These time constants were then compared to numerical simulation in order to extract estimates of the input intensity of the pumping beam. These results are summarized in TABLE III. The polarizer effectively acts as a intensity modulator by manipulating the portions of LCP and RCP light in the input beam.

The obvious improvement to experimental results would be to reduce the systematic fluctuation in the main coil, so that it would not need to be corrected for when comparing quadratic Zeeman splitting levels. An experiment could also be devised

to determine the relationship between polarizer angle and the absorption time constant and thus effective intensity observed in the sample. Finding the point with maximum time constant for fixed intensity would allow one to calibrate the fully LCP rotation of the polarizer, and the polarizer angle to effective intensity relationship could be determined from there.

In terms of numerical improvements, the intensity to absorption decay time constant relationship could be explored much further. A simulation of time constants for a wide log-scale of intensities would be useful as both a reference for experimental work and as a bound on the limits for which this relationship holds.

- ¹B. G. et al, "Chapter 2 - the physics of hyperpolarized gas mri," in *Hyperpolarized and Inert Gas MRI*, edited by M. S. Albert and F. T. Hane (Academic Press, Boston, 2017) pp. 23–46.
- ²R. Bersohn and B. J. Berne, "Chemical physics," in *Encyclopedia of Physical Science and Technology (Third Edition)*, edited by R. A. Meyers (Academic Press, New York, 2003) third edition ed., pp. 739–749.
- ³J. F. Ready, "Chapter 1 - fundamentals of lasers," in *Industrial Applications of Lasers (Second Edition)*, edited by J. F. Ready (Academic Press, San Diego, 1997) second edition ed., pp. 1–30.
- ⁴E. D. Black, *Physics 77 Lab Manual: Optical Pumping*, California Institute of Technology (2004).
- ⁵D. Kleppner, "Rereading einstein on radiation," *Physics Today* **58**, 30–33 (2005), <https://doi.org/10.1063/1.1897520>.
- ⁶A. Kastler, "Optical methods for studying hertzian resonances," *Science* **158**, 214–221 (1967), <https://science.sciencemag.org/content/158/3798/214.full.pdf>.
- ⁷D. Voss, "October 13, 1967: Kastler reviews his nobel-winning work on hertzian resonances in science," *American Physical Society* (2014).
- ⁸J. P. Gordon, H. J. Zeiger, and C. H. Townes, "The maser—new type of microwave amplifier, frequency standard, and spectrometer," *Phys. Rev.* **99**, 1264–1274 (1955).
- ⁹V. M. et al., *ENPH 352: Laboratory Techniques in Physics The Online Edition, Lab Manual*, Department of Physics and Astronomy, University of British Columbia, 6224 Agricultural Road, Vancouver, British Columbia (2021).
- ¹⁰D. A. Steck, *Rubidium 85 D Line Data*, Oregon Center for Optics and Department of Physics, University of Oregon (2019).
- ¹¹D. A. Steck, *Rubidium 85 D Line Data*, Oregon Center for Optics and Department of Physics, University of Oregon (2019).
- ¹²K. Blackard, T. Rappaport, and C. Bostian, "Measurements and models of radio frequency impulsive noise for indoor wireless communications," *IEEE Journal on Selected Areas in Communications* **11**, 991–1001 (1993).
- ¹³N. V. Tkachenko, "Chapter 4 - optical measurements," in *Optical Spectroscopy*, edited by N. V. Tkachenko (Elsevier Science, Amsterdam, 2006) pp. 61–87.
- ¹⁴*Optical Pumping of Rubidium OPI-A: Guide to the Experiment INSTRUCTORS MANUAL*, TeachSpin Inc., 2495 Main Street, Buffalo NY (2002).